



# **JGR** Oceans

#### **RESEARCH ARTICLE**

10.1029/2022JC019281

#### **Key Points:**

- Seasonal mode-1 M<sub>2</sub> internal tides from the Luzon Strait are observed using seasonally subsetted satellite altimetry data from 1993 to 2017
- Westward and eastward M<sub>2</sub> internal tides from the Luzon Strait both demonstrate significant seasonal variation
- The westward internal tides strengthen (weaken) in summer and fall (winter and spring); the opposite is true for the eastward internal tides

#### Correspondence to:

Z. Zhao, zzhao@uw.edu

#### Citation:

Zhao, Z., & Qiu, B. (2023). Seasonal west-east seesaw of M<sub>2</sub> internal tides from the Luzon Strait. *Journal of Geophysical Research: Oceans*, 128, e2022JC019281. https://doi.org/10.1029/2022JC019281

Received 12 SEP 2022 Accepted 8 MAR 2023

#### **Author Contributions:**

Conceptualization: Zhongxiang Zhao Formal analysis: Zhongxiang Zhao, Bo Qiu

Methodology: Zhongxiang Zhao, Bo Qiu Writing – original draft: Zhongxiang Zhao. Bo Oiu

Writing – review & editing: Zhongxiang Zhao. Bo Oiu

# Seasonal West-East Seesaw of M<sub>2</sub> Internal Tides From the Luzon Strait

Zhongxiang Zhao<sup>1</sup> and Bo Qiu<sup>2</sup>

<sup>1</sup>Applied Physics Laboratory and School of Oceanography, University of Washington, Seattle, WA, USA, <sup>2</sup>Department of Oceanography, University of Hawaii at Manoa, Honolulu, HI, USA

**Abstract** Satellite altimetry sea surface height (SSH) measurements from 1993 to 2017 are used to investigate the seasonal variability of mode-1 M<sub>2</sub> internal tides from the Luzon Strait. The 25 years of SSH data are divided into four seasonal subsets, from which four seasonal internal tide models are constructed following the same mapping procedure. Climatological seasonal hydrography in the World Ocean Atlas 2013 is used to calculate two seasonally variable parameters required in the mapping procedure: Wavelength and the transfer function from the SSH amplitude to depth-integrated energy flux. The M<sub>2</sub> internal tides from the Luzon Strait are extracted using propagation direction determined in plane wave analysis. The satellite results show that the westward and eastward M<sub>2</sub> internal tides both demonstrate significant seasonal variation. The westward and eastward internal tides strengthen (weaken) in summer and fall (winter and spring); while the eastward internal tides strengthen (weaken) in winter and spring (summer and fall). We suggest that the seasonal seesaw is mainly determined by ocean stratification and the Kuroshio Current; however, further studies are needed to quantify their relative contributions.

**Plain Language Summary** The generation, propagation, and dissipation of internal tides are affected by a variety of ocean dynamic processes, such that internal tides are subject to temporal variation over timescales from days to decades. A knowledge of their temporal variation is key to advance our understanding of their lifecycle in various ocean environments, their contribution to ocean mixing, and their response to global ocean warming. Two fundamental questions are still poorly understood: How internal tides vary over various timescales? What are the driving mechanisms? Satellite altimetry offers a unique tool for observing internal tides on a global scale from space. Internal tides in different propagation directions in a complex multi-wave field can be separated by plane wave analysis. This paper reveals that  $M_2$  internal tides from the Luzon Strait demonstrate significant seasonal variation and that they are likely modulated by ocean stratification and the Kuroshio Current. This work paves a path to address the above two fundamental scientific questions.

# 1. Introduction

The barotropic tide propagates from the western North Pacific into the South China Sea (SCS) through the Luzon Strait. A fraction of tidal energy is scattered from barotropic to baroclinic motion over two parallel submarine ridges in the Luzon Strait (Figure 1). The baroclinic perturbation propagates away as internal tides, which travel over thousands of kilometers in both the SCS and the western North Pacific (Zhao, 2014). The strong internal tides in the SCS may generate large-amplitude internal solitary waves (Figure 1) (Alford et al., 2015; Li & Farmer, 2011; Zhao et al., 2004). In the past two decades, significant progress has been made in observing and modeling internal tides and internal solitary waves in the northern SCS (Alford et al., 2015; Bai et al., 2019; Buijsman et al., 2014; Chang et al., 2021; Davis et al., 2020; Huang et al., 2016, 2022; Jan et al., 2008; Lien et al., 2014; Mercier et al., 2013; Niwa & Hibiya, 2004; Park & Farmer, 2013; Pickering et al., 2015; Wang et al., 2016; Xie et al., 2021). However, our knowledge of the internal tide variability remains incomplete, though this knowledge is key to understand their generation, propagation, and dissipation. A challenging task for the oceanographic community is to quantify their temporal variation over timescales from days to decades (Buijsman et al., 2017; Colosi & Munk, 2006; DeCarlo et al., 2015; Müller et al., 2012; Savage et al., 2020; Zaron, 2019; Zhai et al., 2020; Zhao, 2016) and their response to global ocean warming and climate change. Toward this goal, this paper focuses on the dominant seasonal variation of mode-1 M, internal tides.

Ray and Zaron (2011) report that the long-range M<sub>2</sub> internal tides in the SCS from the Luzon Strait have large seasonal phase differences, because of different propagation speeds in winter and summer. Zaron (2019)

© 2023. American Geophysical Union. All Rights Reserved.

ZHAO AND OIU 1 of 18

2169291, 2023, 3, Downloaded from https://agupubs.onlinelibrary.wiley.com/doi/10.1029/2022JC019281 by University Of Washington, Wiley Online

**Figure 1.** The study area. (a) Bottom topography. RI, Ryukyu Islands; SCS, South China Sea; TS, Taiwan Strait; WP, western Pacific. Red lines indicate internal solitary waves observed in satellite images (Zhao et al., 2004). (b) Sea surface height (SSH) amplitude of the 25-year-coherent (1993–2017) mode-1 M<sub>2</sub> internal tides from satellite altimetry (this study). Black arrows indicate the AVISO 26-year-mean (1993–2018) geostrophic currents, showing that the Kuroshio Current flows through the source region of internal tides (black box).

shows that the M<sub>2</sub> internal tides from the Luzon Strait demonstrate strong seasonal modulation (fig. 6 therein). However, our understanding of the seasonal variability of internal tides from the Luzon Strait is still poor, as evidenced by the divergent results in previous field and numerical studies. For example, numerical simulations yield contradictory results (Cao et al., 2022; Guo et al., 2020; Jan et al., 2008). Jan et al. (2008) simulate internal tides in the Luzon Strait using summer and winter stratifications, but find no significant seasonal variation. However, Guo et al. (2020) simulate M<sub>2</sub> internal tides using summer and winter stratifications, and show significant and complex differences in internal tide energetics. On the other hand, field measurements also show different seasonal features (Cao et al., 2017; Liu et al., 2015; Xu et al., 2014). Xu et al. (2014) analyze mooring measurements to the west of the Luzon Strait and find that semidiurnal internal tides are seasonally invariant. Liu et al. (2015) analyze mooring measurements at 19.5°N, 120°E, and find strong seasonal variations in both semidiurnal and diurnal internal tides. Cao et al. (2017) show that semidiurnal internal tides are stronger in March-May (spring) and September-November (fall) at two mooring sites close to the Luzon Strait. The controversial results are mainly caused by the challenge of observing the temporal variability of internal tides in a multi-wave internal tide field. The internal tide field around the Luzon Strait is a complex field, consisting of internal tides from multiple generation sites. Unfortunately, mooring measurements at individual sites cannot separate internal tides of different propagation directions and different locations. As demonstrated in this paper, the seasonal variation of internal tides should be studied using the decomposed internal tides by propagation direction.

This paper investigates the seasonal variability of mode-1  $M_2$  internal tides using 25 years of satellite altimetry data from 1993 to 2017. Satellite altimetry has long been used to study internal tides (Ray & Mitchum, 1996, 1997; Ubelmann et al., 2022; Zhao & Alford, 2009; Zhao et al., 2016). Satellite altimetry can observe the horizontal two-dimensional internal tide field, in contrast to mooring measurements at discrete sites. As such, multiple internal tidal waves in different propagation directions can be separately resolved. In a recent paper, Zhao (2021) constructed seasonal mode-1  $M_2$  internal tide models from satellite altimetry and observed significant seasonal variation in the global ocean. The satellite results show that the seasonal variability of internal tides is a function of location, because it is affected by many ocean processes. The seasonal internal tides should be studied region by region. This paper aims to examine the seasonal variability of  $M_2$  internal tides from the Luzon Strait (Figure 1). This region is selected for a dedicated investigation because the Luzon Strait has both energetic internal tides and a complex ocean dynamic environment. The methods developed in this paper are readily applicable to other regions in the global ocean.

The rest of this paper is arranged as follows. Section 2 briefly describes the data and methods used in this paper. Model errors are estimated in Appendix A. Section 3 shows the feasibility and necessity of the multi-wave decomposition of the  $M_2$  internal tide field. Section 4 presents the seasonal variation of  $M_2$  internal tides. Section 5 discusses two driving factors that modulate the internal tide seasonality: ocean stratification and the Kuroshio Current. Section 6 contains conclusions.

ZHAO AND QIU 2 of 18

on Wiley Online Library for rules of use; OA articles are governed by the applicable Creati

## 2. Data and Methods

# 2.1. Satellite Altimetry Data

This work is based on 25 years of sea surface height (SSH) measurements from 1993 to 2017 made by seven exact-repeat altimetry missions: TOPEX/Poseidon, Jason-1, Jason-2, Jason-3, ERS-2, Envisat, and Geosat Follow-On. Their time coverages and ground tracks are shown in Figure 2. The same data have been used to study the southward internal tides in the northeastern SCS (Zhao, 2020) and global seasonal M2 internal tides (Zhao, 2021). The SSH measurements are along four sets of ground tracks. The multi-mission merged data have denser ground tracks and thus higher spatial resolution, which are important for observing mode-1 M2 internal tides with wavelengths of 100–200 km. All SSH measurements have been processed by standard corrections for atmospheric effects, surface wave bias, and geophysical effects (Pujol et al., 2016; Taburet et al., 2019). The ocean barotropic tide, polar tide, solid Earth tide, and loading tide are corrected using theoretical or empirical models (Lyard et al., 2021; Pujol et al., 2016). Unlike previous studies (Ray & Byrne, 2010; Zaron & Ray, 2018), this study makes no mesoscale correction using the AVISO (Archiving, Validation, and Interpretation of Satellite Oceanographic Data) gridded SSH fields. This choice is to avoid that the seasonal variation of internal tides is suppressed by mesoscale correction. We have repeated the analysis using the mesoscale-corrected altimetry data. We obtain similar seasonal features reported here, but with underestimated internal tide amplitudes.

The SSH measurements are divided into four seasonal subsets following the World Ocean Atlas 2013 (WOA13) (Locarnini et al., 2013; Zweng et al., 2013). The seasonal subsetting is as follows: winter (January–March), spring (April–June), summer (July–September), and fall (October–December). This is convenient to match satellite-observed internal tides with the WOA13 seasonal hydrography. Four seasonal internal tide models are constructed using the seasonally subsetted data. Meanwhile, the 25-year-coherent internal tide model is constructed following the same procedure but using the whole data set. The same seasonal subsets have been used to study the seasonal variability of  $M_2$  internal tides on a global scale (Zhao, 2021). However, some mapping parameters are adjusted in this study to better extract internal tides in marginal seas (Section 2.3).

#### 2.2. Internal Tide Parameters

Two key parameters of internal tides are needed in mapping the internal tide and computing energy flux. They are calculated using ocean stratification in the WOA13 climatological seasonal hydrography (Locarnini et al., 2013; Zweng et al., 2013). To account for its seasonal variation, the wavelength is calculated in four seasons. The WOA13 provides annual-mean and four seasonal hydrographies on a spatial grid of 0.25° latitude by 0.25° longitude. Ocean depth is based on the 1′ topography database constructed using in situ and satellite

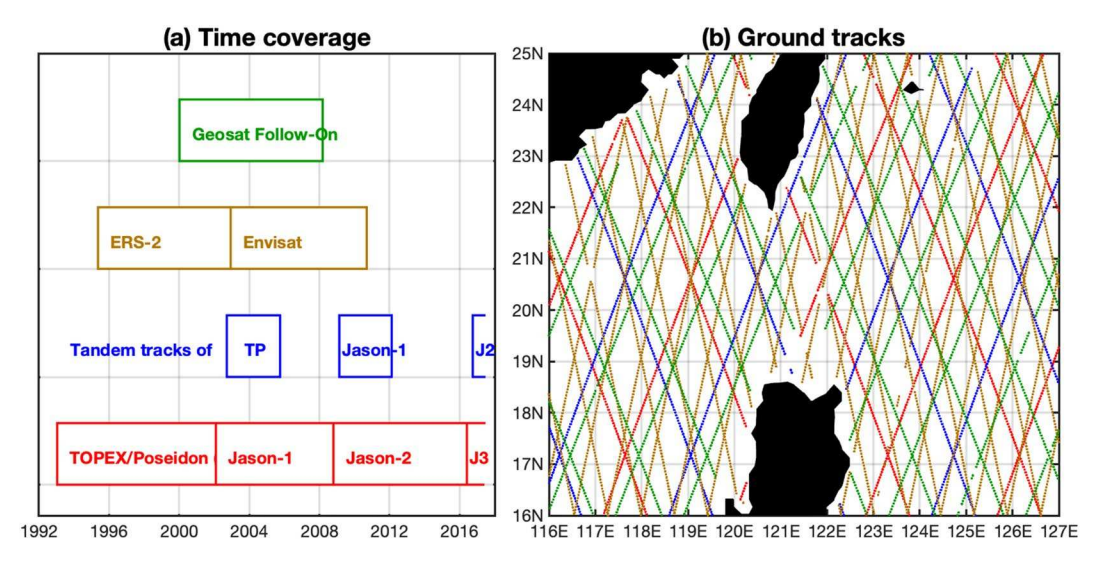


Figure 2. Satellite altimetry data from seven exact-repeat missions. (a) Time coverage. (b) Ground tracks around the Luzon Strait.

ZHAO AND QIU 3 of 18

21699291, 2023, 3, Downloa

measurements (Smith & Sandwell, 1997). At each WOA13 grid point, the ocean depth is obtained by bilinear interpolation. For given ocean depth and stratification profile, the vertical structure and wavelength of mode-1  $M_2$  internal tides are calculated by solving the Sturm-Liouville orthogonal equation (Chelton et al., 1998; Zhao et al., 2016). Note that the seasonal variation of wavelength due to background current is not considered in this study. Figures 3a–3e show the annual-mean and seasonal maps of the wavelength of mode-1  $M_2$  internal tides around the Luzon Strait. It shows that winter and summer have the shortest and longest wavelengths, respectively, consistent with their weakest and strongest ocean stratification. The SCS has shorter wavelengths than the western North Pacific, because the SCS is relatively shallow. Figures 3f–3i show that the percentage changes in opposite seasons (spring vs. fall; summer vs. winter) have similar spatial patterns, but opposite signs.

The transfer function  $(F_n)$  is needed to compute depth-integrated energy flux (F) from the satellite-derived SSH amplitude  $(\eta)$  following  $F = \frac{1}{2}F_n\eta^2$ .  $F_n$  is a function of tidal frequency, mode number, latitude, and ocean stratification (Zhao et al., 2016). To account for its seasonal variation, four sets of  $F_n$  are calculated from the WOA13 climatological seasonal hydrography. The seasonal and annual-mean maps are given in Figures 4a–4e. The results show that the transfer function has significant seasonal variation. It is largest in winter and lowest in summer. For the same SSH amplitude, the  $M_2$  internal tide has greater energy flux in winter than in summer. Inversely, for the same energy flux, the  $M_2$  internal tide has lower SSH amplitude in winter than in summer. Figures 4f–4i show that the season to annual-mean ratios in opposite seasons (spring vs. fall; summer vs. winter) have similar spatial patterns, but reciprocal values.

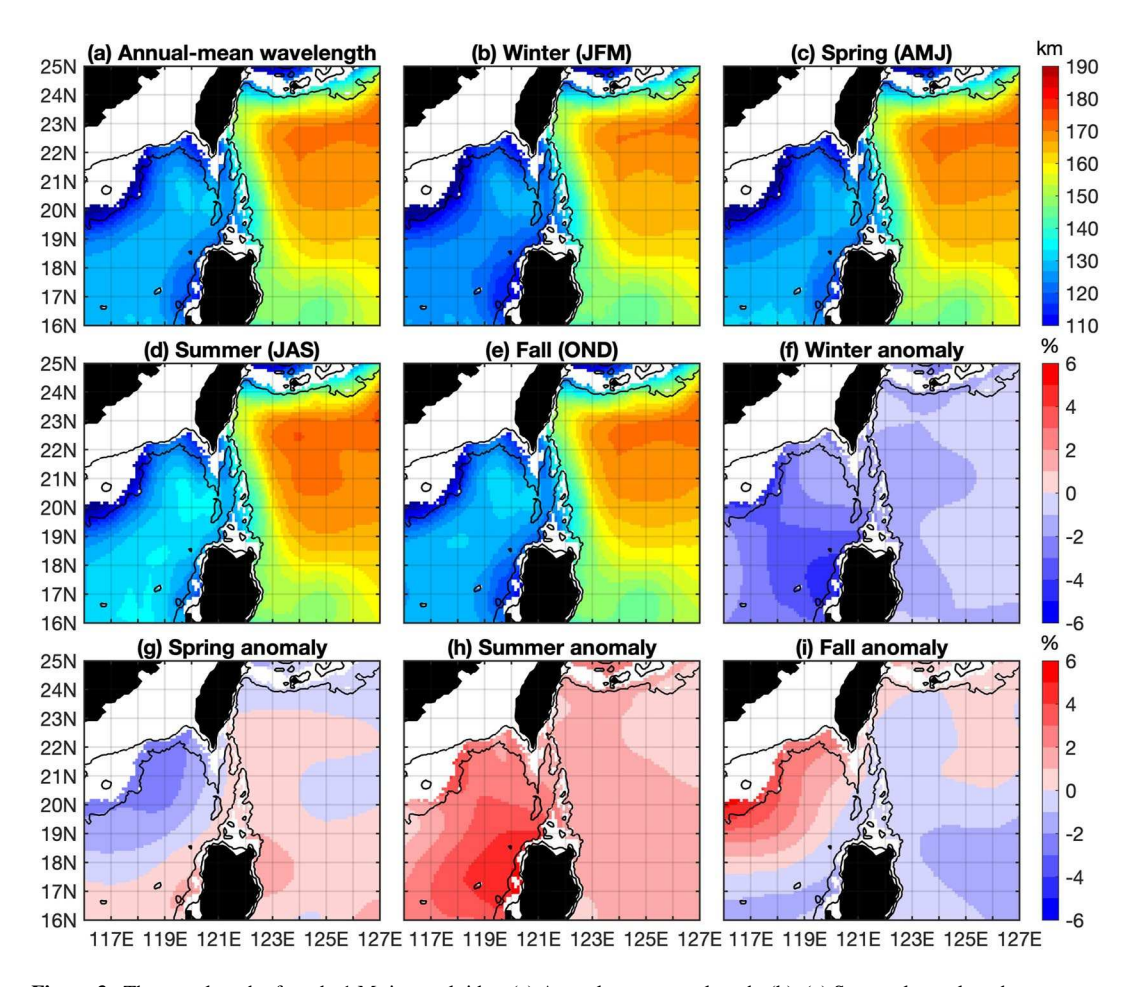


Figure 3. The wavelength of mode-1  $M_2$  internal tides. (a) Annual-mean wavelength. (b)–(e) Seasonal wavelength. (f)–(i) Seasonal percentage change defined as  $(\lambda_k - \lambda_0)/\lambda_0 \times 100\%$ , where  $\lambda_k$  (k = 1-4) and  $\lambda_0$  are the seasonal and annual-mean wavelengths, respectively. Summer (winter) has longer (shorter) wavelengths, because of stronger (weaker) ocean stratification. The 200-m and 2000-m isobath contours are in black.

ZHAO AND OIU 4 of 18

21699291, 2023, 3, Downloaded

The mode-1 M<sub>2</sub> internal tides are mapped following the same mapping procedure as presented in Zhao (2021). It consists of two rounds of plane wave analysis with a spatial bandpass filter in between. The procedure is briefly summarized below. In the first step, mode-1 M<sub>2</sub> internal tides are mapped from the seasonally subsetted data by plane wave analysis. At each grid point, internal waves are determined using all along-track data falling within a 150 km by 150 km window, compared to 200 km by 200 km in Zhao (2021). Five internal tidal waves are determined by least-squares fit and their sum gives the internal tide solution at the grid point. The internal tide field is mapped on a regular grid of 0.1° by 0.1°, compared to 0.2° by 0.2° in Zhao (2021). In the second step, the internal tide field obtained in step 1 is cleaned by a two-dimensional bandpass filter. The filter width is [0.75 1.5] times the regional mean wavelength. The SCS and western Pacific have different wavelengths due to their different depths; therefore, these two regions are bandpass filtered, respectively. In the third step, the internal tide field is decomposed by plane wave analysis. Input is the bandpass-filtered internal tide field obtained in step 2. The parameters are same as those in step 1. In the end, the internal tide field has five internal tidal waves at each grid point. This mapping procedure has been described in previous studies (Zhao, 2020, 2021, 2022). An interested reader is referred to these papers for more details. One known issue with plane wave analysis is that it assumes plane waves in 150 km × 150 km windows. This assumption is invalid for internal tidal waves with curved wavefronts near the generation sources. This issue partly explains why satellite observations underestimate the internal tide energetics, compared to field measurements and numerical simulations (Alford et al., 2015; Huang et al., 2018; Wang et al., 2016). The error associated with the mapping procedure is estimated in Appendix A.

# 3. Interference and Decomposition

#### 3.1. Multi-Wave Interference

Figure 5 shows the four seasonal internal tide fields. Their vector mean (accounting for both amplitude and phase) is almost same as the 25-year-coherent model. All the internal tide models demonstrate complex multiwave interference patterns. In this region,  $M_2$  internal tides come from multiple generation sites, including the Ryukyu Ridge, the Luzon Strait, the Taiwan Strait, seamounts in the western Pacific, and the neighboring continental slope. The superposition of multiple waves leads to standing-wave features. The SSH amplitude is location-dependent, leading to interleaved nodes and antinodes. The co-phase lines are distorted (Figure 5, black lines); therefore, the propagation direction cannot be derived from their normal lines. In fact, the magnitude and direction of energy flux are also a function of location (see fig. 11 in Zhao (2020)). In the multi-wave interference field, it is difficult to quantify the seasonal variation of internal tides from the Luzon Strait.

The four seasonal internal tide fields have some different spatial features, suggesting the seasonal variation of internal tides (Figure 5). The differences can be caused by the following two reasons. First, the internal tide generation may vary seasonally with ocean stratification. Second, the internal tide propagation may vary seasonally, due to the seasonal changes of ocean stratification and circulation. Thus, it is difficult to quantify the seasonal variation of internal tides. In this study, we show that one should separate internal tides from different sources for better studying the internal tide variation.

#### 3.2. Multi-Wave Decomposition

The multi-wave decomposition is conducted using the waves fitted by plane wave analysis at each grid point (Section 2.3). Specifically, the internal tides from the Luzon Strait are extracted by propagation direction. To the west of the Luzon Strait, only internal tides with propagation directions ranging [90° 240°] are retained (Zhao, 2020). To the east, only internal tides with propagation directions ranging [-80° 60°] are retained. The five internal tide models are analyzed respectively by the same method. Figure 6 shows the decomposed outgoing internal tides from the Luzon Strait. In this figure, colors indicate the SSH amplitudes. Black lines indicate the co-phase contours with 180° intervals (half wavelength). Two features confirm that the internal tides are from the Luzon Strait. First, large-amplitude internal tides occur on both sides of the Luzon Strait, suggesting that they are locally generated in the Luzon Strait. Second, the co-phase contours are parallel to the ridges in the Luzon Strait, suggesting that they propagate away from the two ridges.

ZHAO AND QIU 5 of 18

2169291, 2023, 3, Downloaded from https://agupubs.om/inelibrary.wiley.com/doi/10.1029/2022/C019281 by University Of Washington, Wiley Online Library on [15/09/2025]. See the Terms

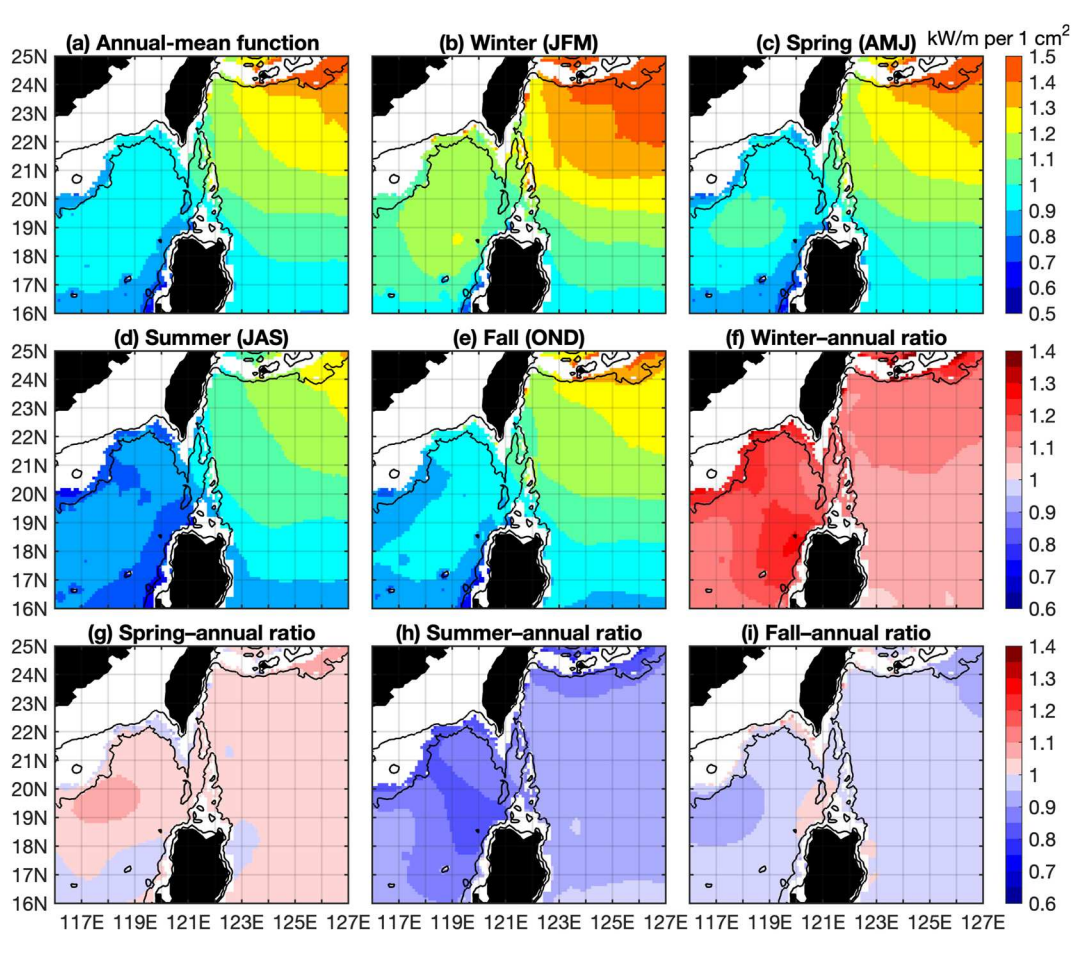


Figure 4. The transfer function from the sea surface height amplitude to depth-integrated energy flux for mode-1  $M_2$  internal tides. (a) Annual-mean function. (b)–(e) Seasonal function. (f)–(i) Ratio of the seasonal to annual-mean function. The 200-m and 2000-m isobath contours are in black.

Figure 6 shows that  $M_2$  internal tides propagate both westward and eastward from the Luzon Strait. In contrast, the internal tide radiation cannot be seen in the multi-wave interference fields (Figure 5). The decomposed fields reveal some well-defined internal tidal beams. Among them, the northwestward (about 165°) beam is remarkable. It propagates toward the Dongsha coral reef, and spawns internal solitary waves during the 500-km propagation (Chang et al., 2021; Zhao, 2014; Zheng et al., 2007). There is a weak southwestward (about 210°) beam in the SCS (Ray & Zaron, 2011; Zaron, 2019). To the east of the Luzon Strait, Figure 6a shows that the dominant propagation direction is southeastward  $(-30^\circ)$  in the 25-year-coherent model. In winter and spring, the eastward internal tides bifurcate into two beams: southeastward  $(-30^\circ)$  and northeastward  $(5-20^\circ)$  (Figures 6b and 6c). In summer and fall, the eastward internal tides are very weak (Figures 6d and 6e).

Figure 6f shows the cross-beam SSH amplitudes along 120°E and 123°E. They are for the westward and eastward beams, respectively. Their cross-beam amplitudes are smooth, because internal tides from other sources have been removed. The internal tidal beams can be identified in cross-beam SSH amplitudes. The two peaks on the westward SSH amplitudes correspond to the northwestward and southwestward beams, respectively. In contrast, the cross-beam SSH amplitudes wiggle in the multi-wave interference fields (Figure 5f).

# 3.3. Interference Versus Decomposition

This section demonstrates the necessity of multi-wave decomposition in the study of internal tide variability. It is illustrated by comparing the seasonal SSH amplitudes in the multi-wave interference and those in the decomposed fields. Figure 7 shows the histograms of point-wise amplitude differences between two pairs of oppopulations.

ZHAO AND QIU 6 of 18

site seasons: summer versus winter and spring versus fall. The study region ranges 19°–22°N, 119°–121.5°E (Figures 5 and 6, green boxes). It is selected to cover the northwestward internal tides from the Luzon Strait. Figures 7a and 7b show the amplitude differences for the multi-wave interference fields (Figure 5) and the decomposed northwestward component (Figure 6), respectively. For the multi-wave interference fields, there are 72% grid points where the internal tides are stronger in summer (vs. winter) and in fall (vs. spring). In contrast, for the decomposed fields, the internal tides are dominantly greater in summer (vs. winter, 98%) and fall (vs. spring, 93%). The contrast is because the former is for the multi-wave superposed component (Figure 7a), while the latter is for the internal tides from the Luzon Strait (Figure 7b). The proper way of quantifying internal tides from the Luzon Strait (other regions as well) is using the multi-wave decomposed components (Figures 6 and 7b).

Figure 7 explains an issue in the study of the temporal variation of internal tides using mooring measurements. In the complex multi-wave field, the mooring measurements contain internal tides originating from multiple generation sites. However, it is difficult (if possible) to resolve internal tides in different propagation directions using station-wise mooring measurements. As described earlier, previous mooring observations of seasonal internal tides from the Luzon Strait have contradictory results (Cao et al., 2017; Liu et al., 2015; Xu et al., 2014), because there is a 28% probability that summer (fall) is weaker than winter (spring) due to multi-wave interference. It is necessary to separate internal tides emanating from the Luzon Strait to study their seasonal or interannual variability. In this regard, satellite altimetry has its advantages over moorings, thanks to its two-dimensional view.

## 4. Seasonal Variation of Internal Tides

Satellite altimetry detects the sea surface manifestation of internal tides. Their energy fluxes can be calculated from the satellite-derived SSH amplitudes (Figure 6) and the transfer function from the WOA13 (Figure 4). In this way, the seasonal variation in the transfer function is taken into account. We have obtained five mode-1  $M_2$  plane waves at each grid point to represent the complex internal tide field. The relation (i.e., the transfer function) between SSH and flux is valid for each simple plane wave (Zaron et al., 2022). Figure 8 shows the resultant 25-year-coherent and seasonal energy fluxes. Colors indicate flux magnitudes. Green arrows indicate flux vectors. It shows both westward and eastward  $M_2$  internal tides from the Luzon Strait. For internal tidal waves with a 25-mm SSH amplitude and  $\pm 7$ -mm errors, the errors in energy flux are estimated to be  $\pm 1.75$  kW/m (Figure 8, error bar). Figure 8c shows unrealistic large energy fluxes around 21°N, 125°E, which are most likely caused by local large SSH errors (see Figure A1c).

Cross-beam integrated energy fluxes are calculated to quantify their strength. The cross-beam sections for the westward and eastward internal tides are along 120°E and 123°E, respectively. These two sections are chosen in the near field of the Luzon Strait, to avoid the influence of mesoscale eddies on internal tides in long-range propagation. But the influence cannot be neglected in the far field (Dunphy & Lamb, 2014; Park & Farmer, 2013; Ponte & Klein, 2015; Zaron & Egbert, 2014). As such, the seasonal variation of the outgoing internal tides can be attributed to generation in the Luzon Strait. The integrated energy fluxes are given in Figure 8. Figure 8f gives a summary of the integrated energy fluxes. One known feature is the asymmetric westward and eastward internal tides (Buijsman et al., 2010; Zhao, 2014). Figure 8a shows that, in the 25-year-coherent model, the westward and eastward energy fluxes are 1.63 and 0.9 GW, consistent with the values (1.53 and 0.9 GW respectively) obtained in Zhao (2014) and qualitatively consistent with numerical simulations (Buijsman et al., 2010).

The westward energy fluxes in winter, spring, summer, and fall are 1.57, 1.17, 1.79, and 1.90 GW, respectively. Spring and fall have the weakest and strongest westward internal tides, respectively, with the latter being about 60% greater than the former. The eastward energy fluxes in winter, spring, summer, and fall are 1.54, 1.23, 0.73, and 0.75 GW, respectively. Summer and winter have the weakest and strongest eastward internal tides, respectively, with the winter radiation about twice the summer radiation. The westward and eastward internal tides both demonstrate significant seasonal variation (Figure 8). The total (westward plus eastward) energy fluxes in winter, spring, summer, and fall are 3.11, 2.40, 2.52, and 2.65 GW, respectively. The result suggests that the internal tide generation is strongest in winter and weakest in spring. In winter, the converted internal tide energy is equally partitioned into the westward and eastward components. In spring, on the contrary, about two thirds of the converted internal tide energy is transported away with the westward internal tides.

The seasonal variation of internal tides is further examined in terms of seasonal flux anomaly. Here, the seasonal flux anomalies are calculated for the westward and eastward internal tides, respectively. After subtracting their

ZHAO AND QIU 7 of 18

2169291, 2023, 3, Downloaded from https://agupubs.om/inelibrary.wiley.com/doi/10.1029/2022/C019281 by University Of Washington, Wiley Online Library on [15/09/2025]. See the Terms

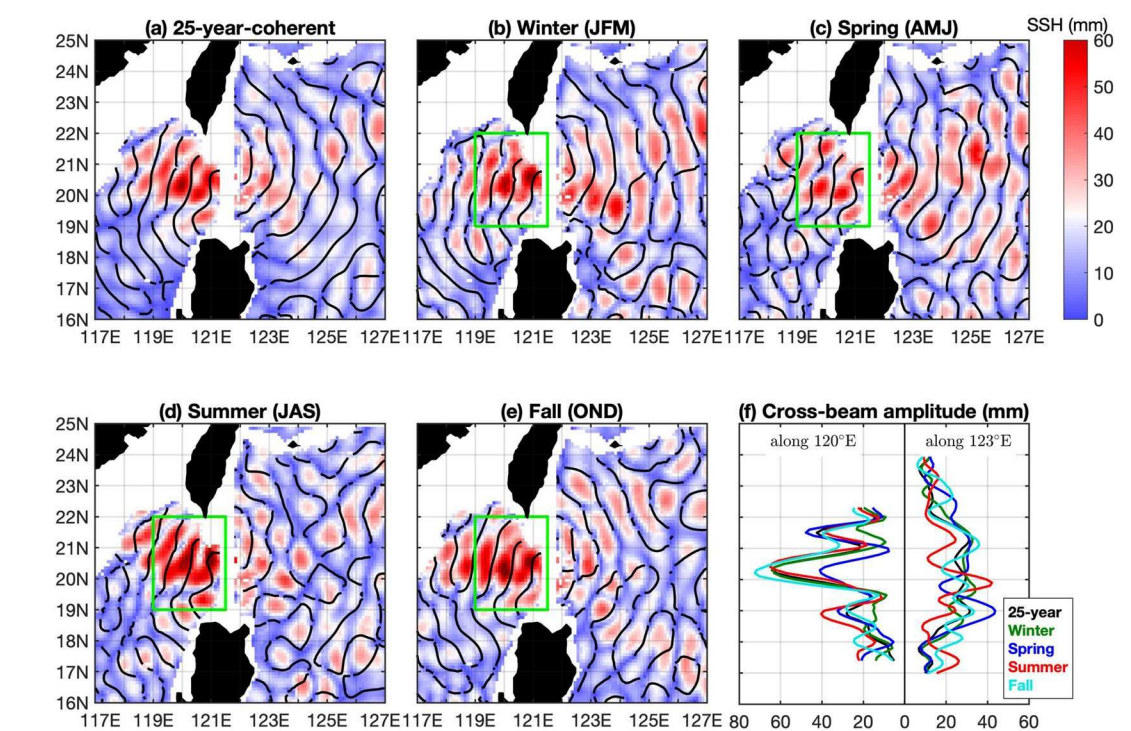


Figure 5. Mode-1  $M_2$  internal tides around the Luzon Strait. Colors indicate sea surface height (SSH) amplitudes. Black lines indicate co-phase contours with an interval of 180° (half wavelength). (a) 25-year-coherent. (b) Winter. (c) Spring. (d) Summer. (e) Fall. All models show a multi-wave interference pattern, due to their multiple generation sources. (f) SSH amplitudes along 120°E and 123°E.

mean energy fluxes, the seasonal flux anomalies can better describe their seasonal variation. The seasonal mean westward energy flux is 1.61 GW; therefore, the westward seasonal flux anomalies are -0.04, -0.44, 0.18, and 0.29 GW, respectively. Similarly, the eastward seasonal flux anomalies are calculated to be 0.48, 0.17, -0.33, and -0.31 GW, respectively. Figure 9a shows the resultant seasonal flux anomalies. It has one remarkable feature: The westward internal tides strengthen (weaken) in summer and fall (winter and spring); on the contrary, the eastward internal tides strengthen (weaken) in winter and fall (summer and fall). In other words, Figure 9a demonstrates a seesaw feature, that is, the westward and eastward internal tides rise and fall seasonally. More internal tide energy is transported westward into the SCS in summer and fall, while more internal tide energy is transported eastward into the western Pacific in winter and spring. The season variation may affect the internal tide-driven ocean mixing around the Luzon Strait.

# 5. Discussion: Driving Factors

The  $M_2$  barotropic tide group contains a few tidal constituents centering around  $M_2$ , and their superposition causes seasonal variability of the  $M_2$  tide group (Ray, 2022, table 1 therein). Some studies report that the seasonal variation of internal tides is closely correlated to the barotropic tidal forcing (Liu et al., 2015). The seasonality of the barotropic tide is usually weak and cannot explain the large seasonal cycle in internal tides. Note that some ocean regions demonstrate strong seasonal variation of the barotropic tide (Bij de Vaate et al., 2021; Müller et al., 2014). Ray (2022) points out that both tide and internal tide can be modulated by climate processes such as ocean stratification, ice cover, and river discharge. In addition, incoming internal tides from the western North Pacific are weak; therefore, their influence is not examined in this study (Ubelmann et al., 2022; Zaron, 2019; Zhao, 2021). The Luzon Strait has a complex ocean dynamic environment, where the internal tide generation is affected by a variety of factors, including ocean stratification, bottom slope, double-ridge resonance, the Earth's rotation, the Kuroshio Current, and incoming internal tides (Buijsman et al., 2014; Jan et al., 2008, 2012; Kelly & Nash, 2010; Kerry et al., 2013; Mercier et al., 2013; Xie et al., 2021). In this study, we discuss two climate-driven processes. We will examine the influence of ocean stratification and the Kuroshio Current, because both of them have pronounced seasonal cycles (Kim et al., 2004; Nan et al., 2015; Qiu & Lukas, 1996; Wu et al., 2017; Yuan et al., 2006).

ZHAO AND QIU 8 of 18

21699291, 2023, 3, Downloaded from https://agupubs.onlinelibrary.wiley.com/doi/10.1029/2022LC019281 by University Of Washington, Wiley Online Library on [15/09/2025]. See the Terms and Conditional Conditions of the Conditional Conditional Conditions of the Conditional C

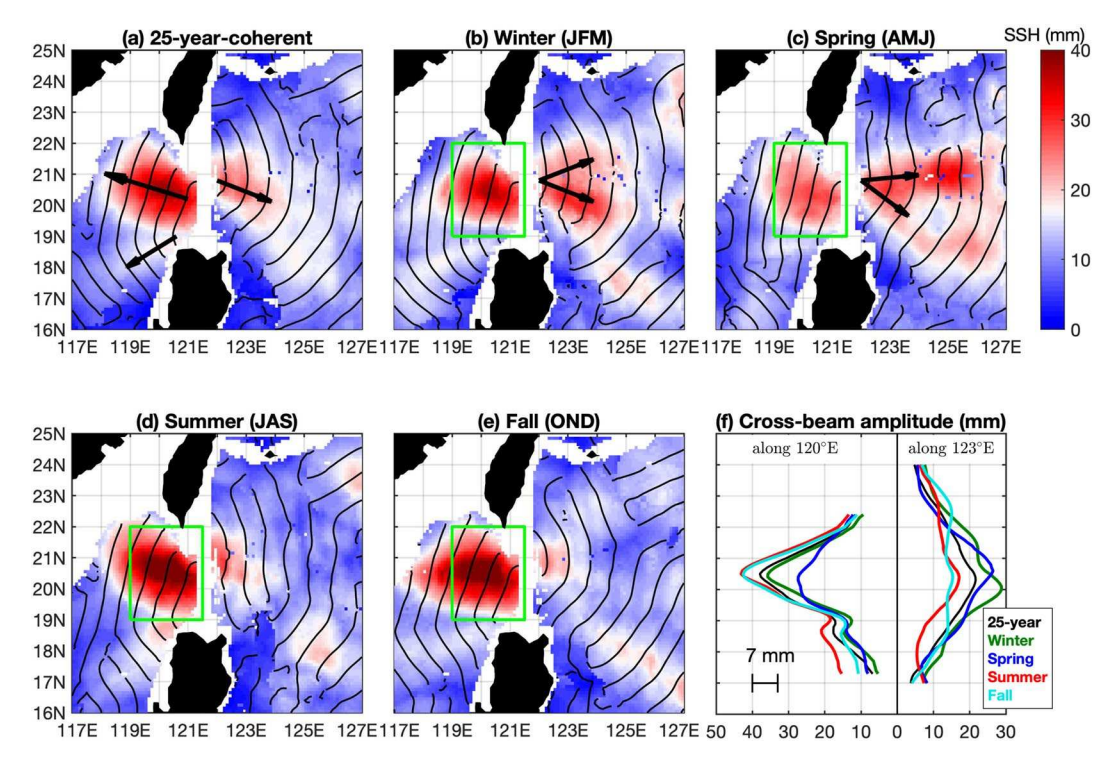


**Figure 6.**  $M_2$  internal tides from the Luzon Strait. Westward (90°-240°) and eastward (-80° to 60°) internal tides are separately extracted. Black lines indicate co-phase contours with an interval of 180° (half wavelength). Internal tidal beams are labeled using black arrows. (a) 25-year-coherent. (b) Winter. (c) Spring. (d) Summer. (e) Fall. (f) Cross-beam sea surface height (SSH) amplitudes along 120°E (westward) and 123°E (eastward). The 7-mm error is estimated in Appendix A.

# 5.1. Ocean Stratification

Ocean stratification is quantified in terms of buoyancy frequency defined as  $N(z) = \left(-\frac{g}{\rho_0} \frac{d\rho(z)}{dz}\right)^{1/2}$ , where g is the gravity constant,  $\rho_0$  the reference density, and  $\rho(z)$  the potential density. The seasonal N(z) profiles are from the WOA13 seasonal hydrography. Figure 10c shows the seasonal N(z) profiles averaged in region 19°–21.5°N,

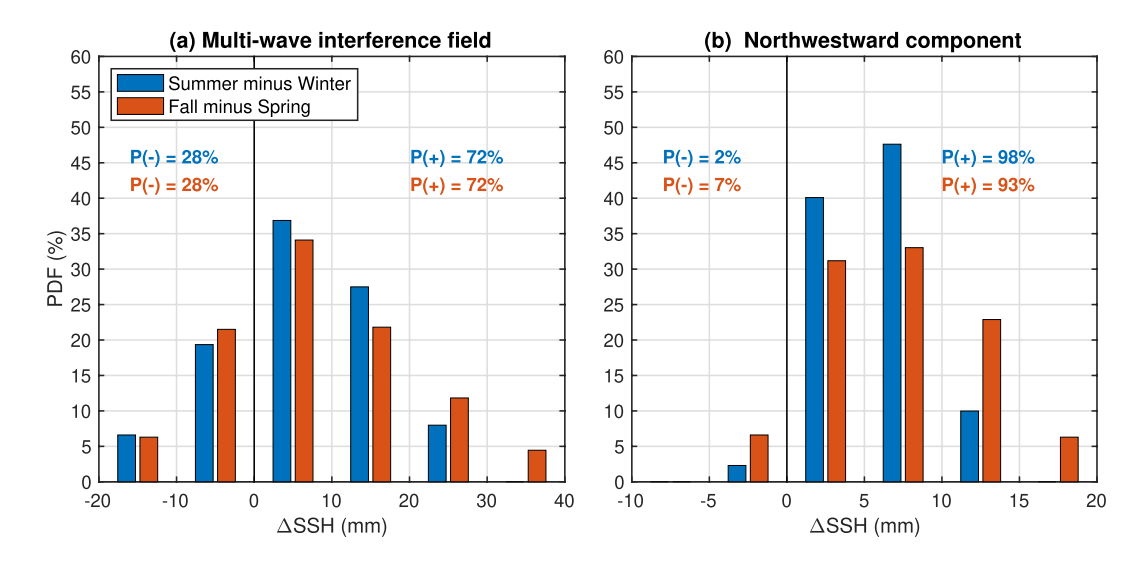


Figure 7. Seasonal differences of the sea surface height (SSH) amplitude of  $M_2$  internal tides from the Luzon Strait. Shown are the probability density functions (PDFs) of point-wise differences in region  $19^{\circ}-22^{\circ}N$ ,  $119^{\circ}-121.5^{\circ}E$  (Figures 5 and 6, green box). (a) For the multi-wave interference field as shown in Figure 5. (b) For the northwestward internal tides as shown in Figure 6. P(-) and P(+) give the accumulated percentages of negative and positive values.

ZHAO AND QIU 9 of 18

17N

2169291, 2023, 3, Downloaded from https://agupubs.onlinelibrary.wiley.com/doi/10.1029/2022/C019281 by University Of Washington, Wiley Online Library on [15/09/2025]. See the Terms

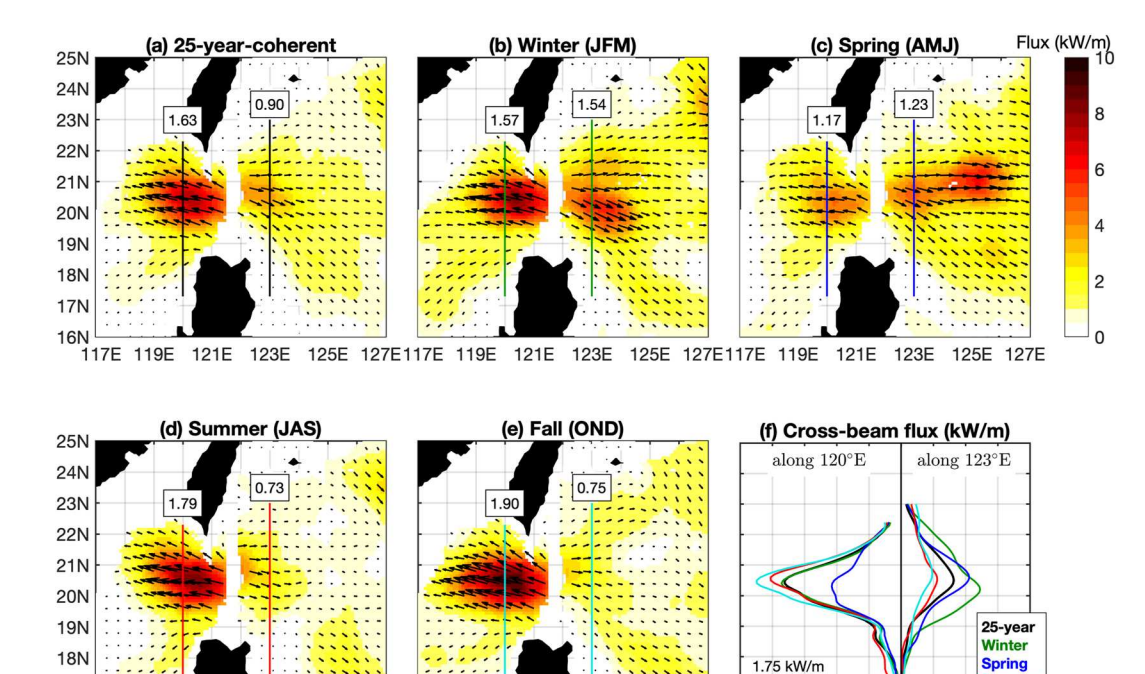
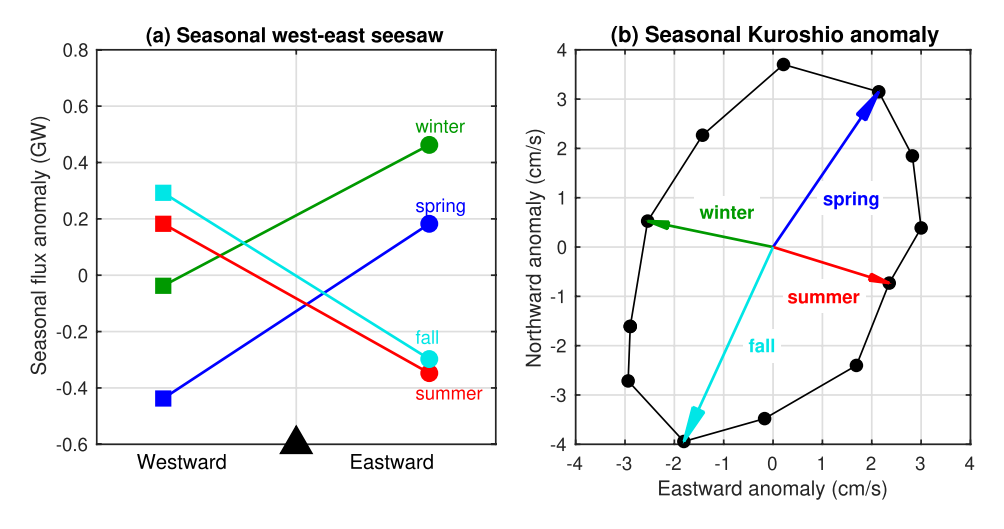


Figure 8. Energy flux of mode-1  $M_2$  internal tides from the Luzon Strait. (a) 25-year-coherent. (b) Winter. (c) Spring. (d) Summer. (e) Fall. Colors and arrows indicate the magnitude and direction of internal tides, respectively. (f) Cross-beam energy fluxes along 120°E (westward) and 123°E (eastward). In (a)–(e), the cross-beam integrated energy fluxes are given in GW (1 GW =  $10^9$  W). The error bar is estimated using a 25-mm sea surface height (SSH) amplitude and a 7-mm error (see Appendix A).

119E 121E 123E 125E 127E117E 119E 121E 123E 125E 127E 10 8

 $120.5^{\circ}$ – $122.5^{\circ}$ E. This region is chosen in that it covers the major generation sites of  $M_2$  internal tides in the Luzon Strait. The figure shows only the stratification profile in the upper 500 m, because the lower layer has weak seasonal variation. Figures 10d–10g give the latitude-depth sections from  $117^{\circ}$ E to  $127^{\circ}$ E along  $20^{\circ}$ N. Figure 10h shows the seasonal buoyancy frequency averaged over 0–500 m. For direct comparison, Figure 10h shows the seasonal  $M_2$  internal tides from the Luzon Strait.



**Figure 9.** Seasonal west-east seesaw of mode-1 M<sub>2</sub> internal tides from the Luzon Strait. (a) Seasonal west-east seesaw. (b) Seasonal variation of the Kuroshio Current. Black dots indicate 3-month-mean Kuroshio Current anomalies. Arrows highlight the four seasonal anomalies as shown in Figure 11.

ZHAO AND QIU 10 of 18

2169291, 2023, 3, Downloaded from https://agupubs.onlinelibrary.wiley.com/doi/10.1029/2022/C019281 by University Of Washington, Wiley Online Library on [15/09/2025]. See the Terms

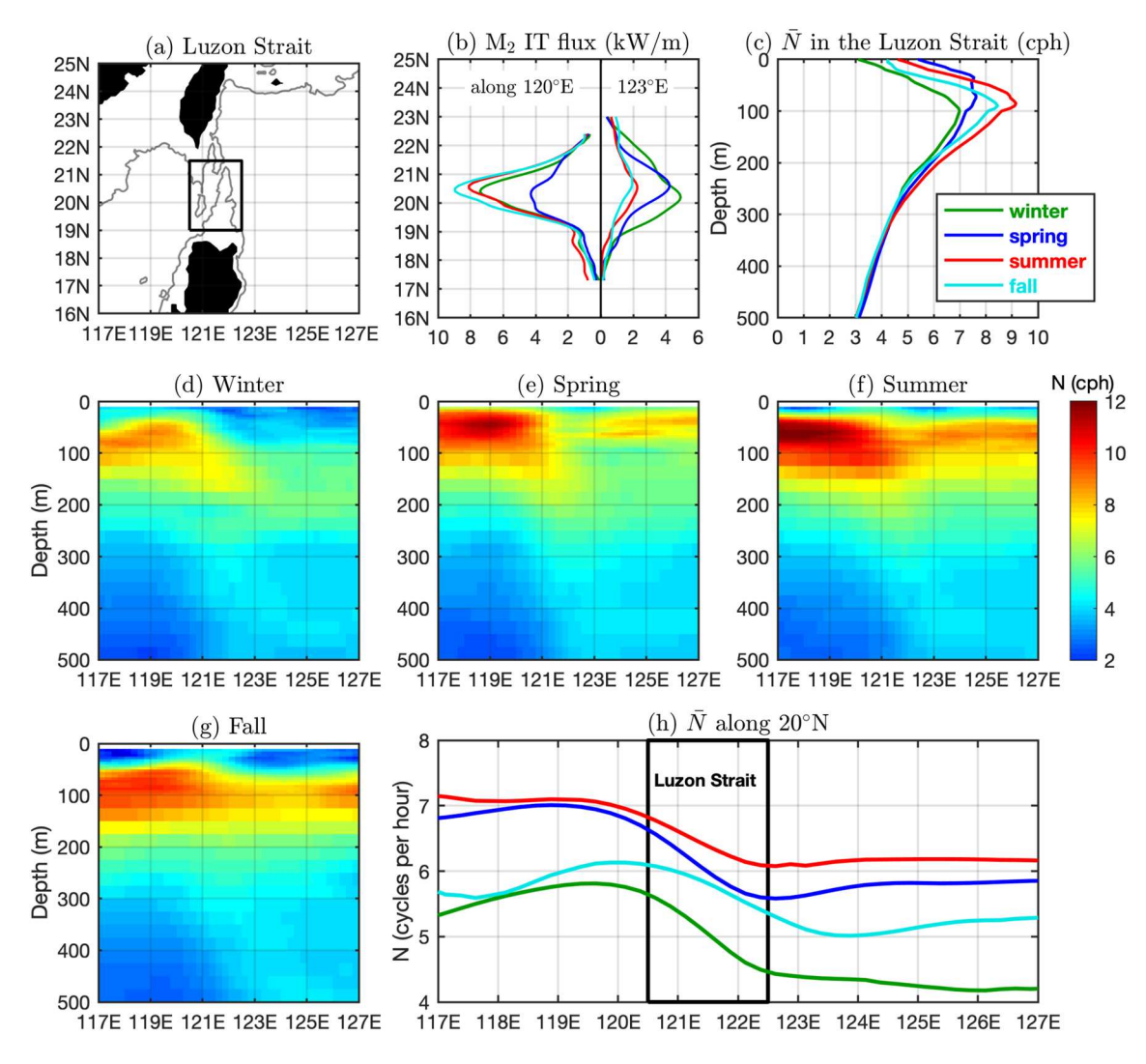


Figure 10.  $M_2$  internal tides and ocean stratification. (a) The Luzon Strait. (b) Seasonal  $M_2$  internal tides. (c) Seasonal buoyancy frequency profiles averaged in region  $19^{\circ}-21.5^{\circ}N$ ,  $120.5^{\circ}-122.5^{\circ}E$  (box in (a)). (d)–(g) Seasonal longitude-depth buoyancy frequency along  $20^{\circ}N$ . (h) Seasonal depth-averaged (0–500 m) buoyancy frequency along  $20^{\circ}N$ . Ocean stratification below 500 m has weak seasonal variation (not shown).

Figure 10 shows that the Luzon Strait has a complex stratification structure, due to (a) its connection of two different water bodies and (b) the presence of the Kuroshio Current (Section 5.2). The ocean stratification is stronger in summer and fall (Figure 10c, red and cyan) than in winter and spring (green and blue). This feature agrees with the seasonal variation of the westward flux, which is stronger in summer and fall, and weaker in winter and spring (Figure 10b). Buijsman et al. (2010, 2014) show that time-varying ocean stratification can change the internal tide wavelength, which can modulate the double-ridge resonance in the Luzon Strait. Therefore, ocean stratification can influence the internal tide generation and westward-eastward partition. However, Figure 10c shows that ocean stratification is strongest in summer and weakest in winter. In contrast, the satellite results show that the  $M_2$  internal tides are strongest in winter and weakest in spring. Furthermore, neither the westward nor the eastward  $M_2$  internal tides increase/decrease with the strengthening/weakening of ocean stratification. Specifically, the westward  $M_2$  internal tides are weakest in spring; in contrast, the spring stratification is stronger than winter and fall; the eastward  $M_2$  internal tides are weakest in summer; in contrast, the summer stratification is strongest. These features suggest that the internal tide generation and ocean stratification do not have a linear relation. In other words, the seasonal variation of ocean stratification alone cannot fully explain the seasonal  $M_2$  internal tides or their west-east seesaw.

ZHAO AND QIU 11 of 18

21699291, 2023, 3, Downloaded from https://agupubs.onlinelibrary.wiley.com/doi/10.1029/2022/C019281 by University Of Washington, Wiley Online Library on [15/09/2025]. See the Terms

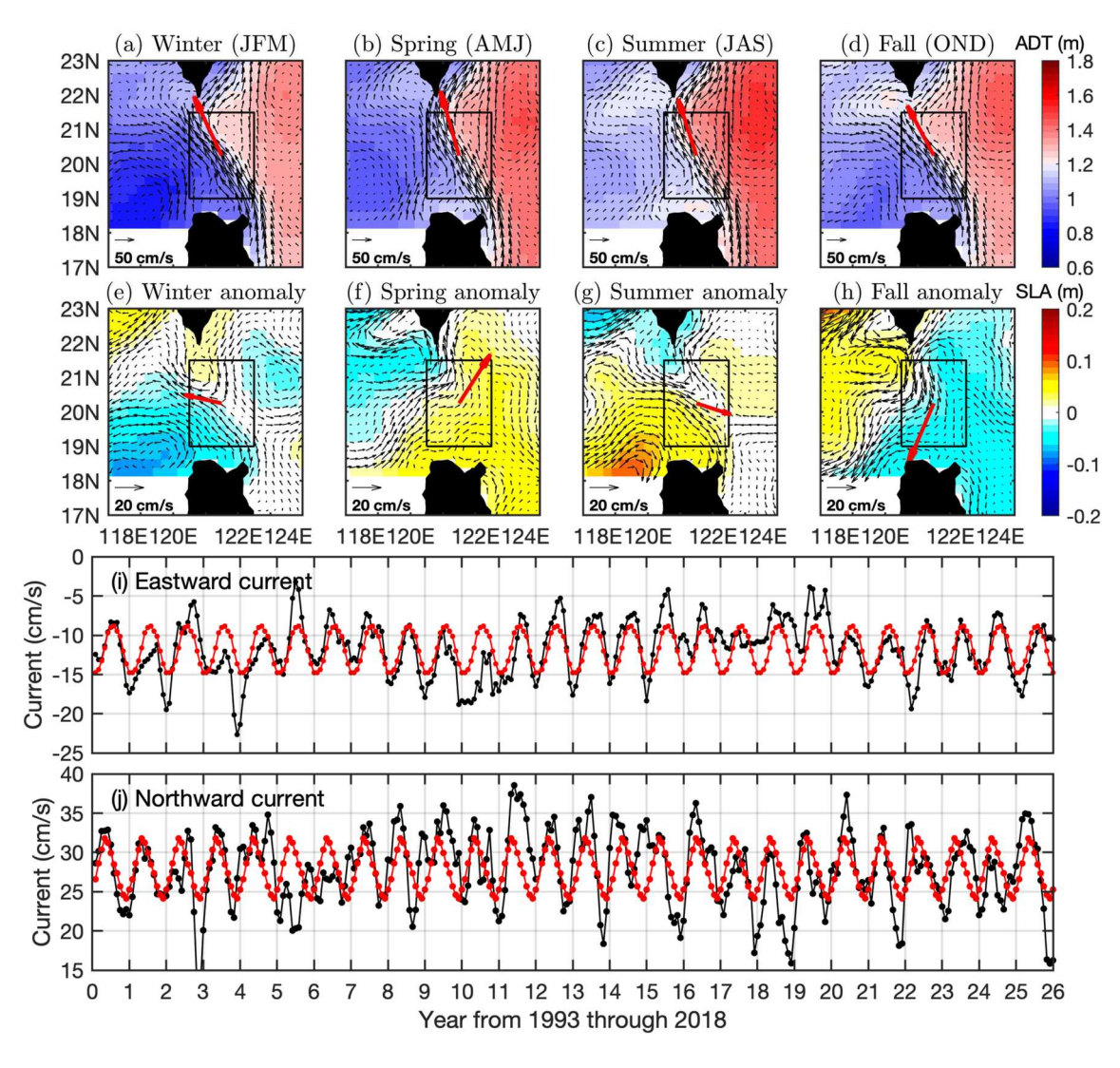


Figure 11. Seasonal variation of the Kuroshio Current. (a)–(d) Absolute dynamic topography (ADT, colors) and geostrophic current (arrows). The bold red arrows show mean currents (amplified five times) averaged in the Luzon Strait (black box). (e)–(h) Sea level anomaly (SLA, colors) and geostrophic current anomaly (arrows). The bold red arrows show the anomalies (amplified 10 times) in the Luzon Strait. (i) Eastward current and (j) northward current averaged in region 19°–21.5°N, 120.5°–122.5°E (black box). The black and red lines indicate the original time series and their seasonal cycles, respectively.

Previous satellite and field observations show that the internal solitary wave (ISW) activities around Dongsha are particularly weak in winter (Huang et al., 2022; Zheng et al., 2007). In contrast, our satellite altimetric results show that the westward  $M_2$  internal tides are stronger in winter than in spring (Figure 10a). This contradictory feature can be explained by the ocean stratification in the northern SCS (Figure 10). Note that ISWs are generated by the nonlinear steepening of internal tides propagating from the Luzon Strait to Dongsha (Alford et al., 2015; Li & Farmer, 2011). Figure 10h shows that the ocean stratification in the SCS is stronger in spring than in winter. The weak stratification in winter does not favor the evolution from internal tides to ISWs; while the strong stratification in spring facilitates the generation of ISWs.

#### 5.2. Kuroshio Current

The Kuroshio Current is the northward flowing western boundary current in the western North Pacific. It originates from the northward limb of the bifurcated North Equatorial Current at around 15.5°N (Kim et al., 2004; Qiu & Lukas, 1996). The Kuroshio flows along the east coast of Luzon and Taiwan, and frequently intrudes into the SCS through the Luzon Strait. Here, its seasonal variation is quantified using 26 years of AVISO gridded SSH fields from 1993 through 2018. The AVISO fields are gridded daily in time and 0.25° by 0.25° in the horizontal.

ZHAO AND QIU 12 of 18

The AVISO fields are divided into four seasonal subsets following the convention in the WOA13 (Section 2.1). Figures 11a-11d show the seasonal maps of absolute dynamic topography (ADT) and geostrophic current. For each season, the mean current in the Luzon Strait is averaged in region  $19^{\circ}-21.5^{\circ}N$ ,  $120.5^{\circ}-122.5^{\circ}E$  (black box) and indicated using a bold red arrow. The seasonal variation is weak, compared to the mean current. To highlight its seasonal variation, Figures 11e-11h show the seasonal maps of sea level anomaly and geostrophic current anomaly, which are obtained by subtracting corresponding annual means. The results show that the northward current has positive anomaly in spring and negative anomaly in fall; while the westward current has positive anomaly in winter and negative anomaly in summer. Figures 11i and 11j show the monthly time series of the eastward and northward currents (black lines) that are averaged in region  $19^{\circ}-21.5^{\circ}N$ ,  $120.5^{\circ}-122.5^{\circ}E$ . The red lines indicate their seasonal cycles, which are obtained by averaging the 26 years of geostrophic currents month by month. The results show that the Kuroshio Current in the Luzon Strait has a pronounced seasonal cycle. The northward current has a seasonal variation of  $\pm 4$  cm/s, and the westward current has a seasonal variation of  $\pm 3$  cm/s.

Figure 9 compares the seasonal west-east seesaw with the seasonal Kuroshio anomaly, both of which have pronounced seasonal cycles. It shows that the positive northward Kuroshio anomalies in winter and spring correspond to negative (positive) westward (eastward) flux anomalies. On the contrary, the negative northward Kuroshio anomalies in summer and fall correspond to positive (negative) westward (eastward) flux anomalies. The good relation leads to the hypothesis that the seasonal variation of M<sub>2</sub> internal tides is modulated by the Kuroshio Current. This hypothesis has its theoretical and numerical evidence. For example, Lamb and Dunphy (2018) suggest that the surface trapped flow affects tide-topography interactions and leads to asymmetric energy flux and larger upstream flux. Similarly, Shakespeare and Hogg (2019) suggest that the background current cause the asymmetry between the upstream and downstream internal tides and larger upstream momentum. Numerical simulations of the Luzon Strait also show that the Kuroshio can significantly affect the generation of internal tides in the Luzon Strait (Cao et al., 2022; Jan et al., 2012; Xu et al., 2021). However, these theoretical and numerical studies usually employ idealized Kuroshio conditions, and thus cannot fully reproduce the seasonal internal tides observed in this study. Future numerical simulations with realistic stratification and Kuroshio Current are needed to test this hypothesis. In particular, Jan et al. (2012) suggest that the influence of the Kuroshio Current on internal tides may be caused by pycnocline sloping, relative vorticity, current shear, density front, or flow advection. Dedicated numerical simulations are needed to discriminate these dynamic factors.

# 6. Conclusions

This paper shows that the seasonal variability of mode-1  $M_2$  internal tides from the Luzon Straits can be investigated using 25 years of satellite altimetry data from 1993 to 2017. The satellite SSH data are divided into four seasonal subsets, from which four seasonal  $M_2$  internal tide models are constructed. To account for the seasonal variation of ocean stratification, climatological seasonal hydrography in the WOA13 provides two seasonally variable parameters in the mapping procedure: Wavelength and the transfer function from the SSH amplitude to depth-integrated energy flux. The model errors are much lower than the internal tide signals, allowing us to study their seasonal variation.

The  $M_2$  internal tides around the Luzon Strait are from multiple generation sources, including the Luzon Strait, the Ryukyu Islands, the Taiwan Strait, the neighboring continental slope, and seamounts in the western North Pacific. To study the internal tide radiation from the Luzon Strait, we separately resolve internal tides from different generation sources. The westward and eastward  $M_2$  internal tides from the Luzon Strait are extracted utilizing their propagation directions determined by plane wave analysis. The decomposition yields a clear picture of the internal tide field. In contrast, station-wise mooring measurements cannot resolve internal tides from different sources; therefore, it is challenging to study the seasonal variation of internal tides using a small number of moorings.

The mode-1  $\rm M_2$  internal tides from the Luzon Strait demonstrate significant seasonal variation. The westward internal tides are strongest in fall (1.90 GW) and weakest in spring (1.17 GW), with the former being about 60% greater than the latter. The eastward internal tides are strongest in winter (1.54 GW) and weakest in summer (0.73 GW), with the former being about two times the latter. In particular, the internal tides from the Luzon Strait demonstrate a seasonal west-east seesaw feature: The westward internal tides strengthen (weaken) in summer and fall (winter and fall); while the eastward internal tides strengthen (weaken) in winter and fall (summer and fall). This finding has important implications for parameterizing internal tide-driven ocean mixing.

ZHAO AND QIU 13 of 18

This work explores the potential role of ocean stratification and the Kuroshio Current on the internal tide variation in the Luzon Strait. Ocean stratification is prerequisite for the generation of internal tides, but its seasonal variation alone cannot fully explain the seasonal west-east seesaw of internal tides. The Kuroshio Current plays an important role in modulating the internal tide generation in the Luzon Strait (Jan et al., 2012). The seasonal west-east seesaw may be controlled by the seasonally meandering Kuroshio Current. This hypothesis should be testified using dedicated numerical simulations with realistic Kuroshio Current. This hypothesis suggests that a strong Kuroshio Current would lead to weaker westward internal tide and stronger eastward internal tides. This inference is useful for forecasting the ISW activities with global ocean warming and enhanced Kuroshio Current.

Satellite altimetry data can be used to further explore the internal tides from the Luzon Strait. First, they can be used to study the seasonal variation of diurnal  $O_1$  and  $K_1$  internal tides. This task is challenging because diurnal internal tides have long wavelengths (300–400 km), compared to the small dimensions of the northeastern SCS and Luzon Strait. The authors have repeated the procedure for diurnal internal tides, but the resultant internal tides have large errors. Second, they can be used to study the monthly variation of internal tides. The authors have repeated the procedure for 12 monthly subsetted datasets. The resultant internal tides have larger errors, because of the shorter subsets. The strong westward internal tides can be seen in the monthly models, but the weak eastward internal tides are buried in noise. Fortunately, the methods developed in this paper are readily applicable, whenever sufficient satellite data are accumulated in the future.

# **Appendix A: Model Errors**

We estimate errors in the  $M_2$  internal tide models using background internal tide fields. One prerequisite parameter in our mapping procedure is the period of the target internal tides. The  $M_2$  internal tide fields are constructed with the  $M_2$  tidal period (about 12.4206 hr). In contrast, the background internal tide fields are constructed using the same satellite data and following the same mapping procedure, but with two background tidal periods. They are  $\pm 3$  min different from the  $M_2$  period. These two periods are chosen, because there are no major tidal constituents at these periods. They are on two sides of  $M_2$  to avoid possible systematic bias in the internal tide background. For each season, two background internal tide fields are constructed with  $M_2 \pm 3$  min, and their scalar mean field is calculated for further analysis. (Their vector mean, with phase involved, would lead to underestimated amplitudes by a factor of  $\sqrt{2}$ .) The background internal tides are not affected by the strong  $M_2$  internal tides and other constituents in the  $M_2$  group ( $\gamma_2$ ,  $MA_2$ ,  $MB_2$ , and  $MKS_2$ ), because the 25-year-long satellite data have high-frequency resolution (better than 0.2 cycles per year). To confirm that the background internal tide fields are mostly errors, we calculate the correlation coefficients between the two background fields and their corresponding  $M_2$  fields. The correlation coefficients are around 0.1 in all four seasons, suggesting that the background and  $M_2$  internal tide fields are independent.

The resulting seasonal background internal tide fields are shown in Figure A1. Note that the seasonal  $M_2$  internal tide fields are shown in Figure 6. For comparison, Figures A1 and 6 show SSH amplitudes in the same format. All models have been divided into westward (90°–240°) and eastward (-80° to 60°) components from the Luzon Strait. The results show that the background fields have much lower SSH amplitudes than the  $M_2$  fields, as expected. Figure A1f shows that the cross-beam SSH amplitudes are around 7 mm in the background fields. In contrast, Figure 6f shows that they are around 15–30 mm in the  $M_2$  fields. Figure A2 shows the histograms of the model errors estimated in Figure A1. It shows that there are not much differences between the eastward and westward components. For both components, the errors in the 25-year-coherent models peak at 3 mm, and those in the four seasonal models peak around 6–8 mm. We find that the largest errors (up to 15 mm) appear in the summer eastward component (Figure A1d), which is consistent with the strongest mesoscale motions in the summer in this region (Chen & Qiu, 2021) (see their fig. 7).

In the literature, a similar strategy has been used to estimate errors in barotropic tides or tidal variations. For example, Ray and Susanto (2016) studied the spring-neap tidal cycles (MSf and Mf) of tidal mixing in the Indonesian Seas using satellite sea surface temperature data. They quantify errors using the (temperature) amplitudes of a few false tides in the vicinity of MSf and Mf lines. Recently, Zaron et al. (2023) studied the fortnightly variability of Chl a in the Indonesian Seas using satellite sea surface color data. Their model errors are estimated using the (Chl a concentration) amplitudes at several fake tidal frequencies near the real constituents  $S_a$  and MSf. This method (background tide, false tide, or fake tide) is particularly useful when we do tidal analysis on data that are irregularly sampled in space and/or time.

ZHAO AND QIU 14 of 18

2169291, 2023, 3, Downloaded from https://agupubs.onlinelibrary.wiley.com/doi/10.1029/2022/C019281 by University Of Washington, Wiley Online Library on [1509/2025]. See the Terms and Conditions (https://onlinelibrary.wiley.com/errms-

and-conditions) on Wiley Online Library for rules of use; OA articles are governed by the applicable Creative Commons Licenso

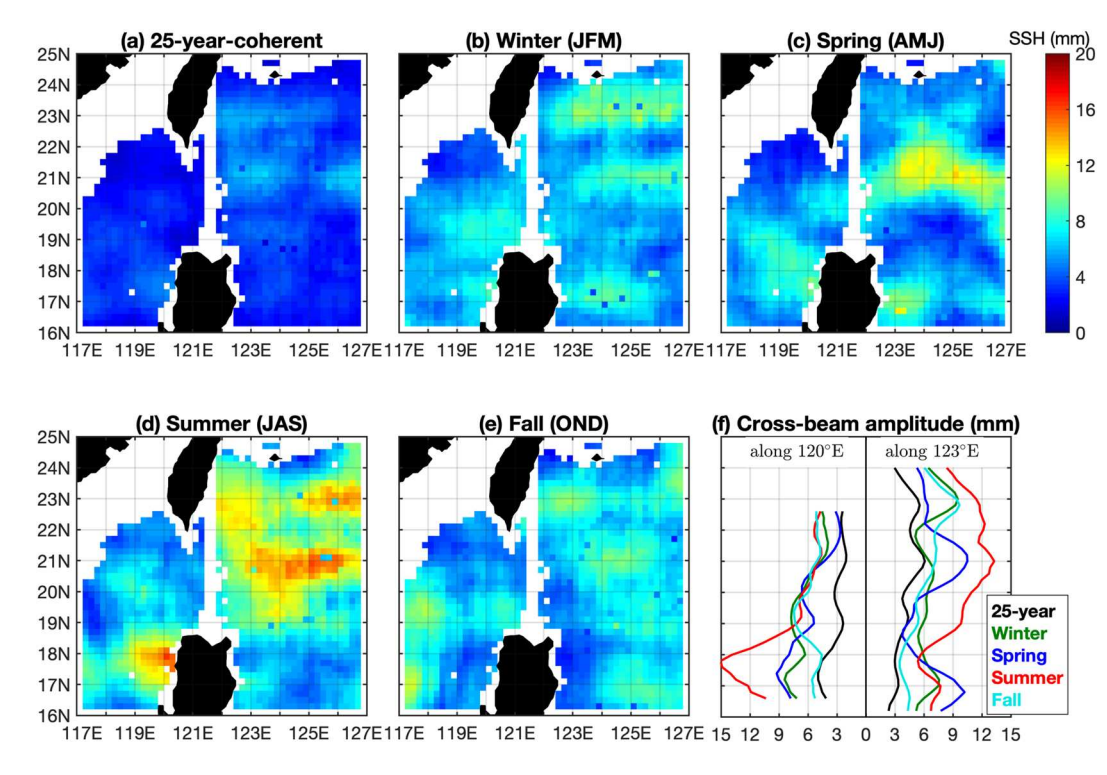
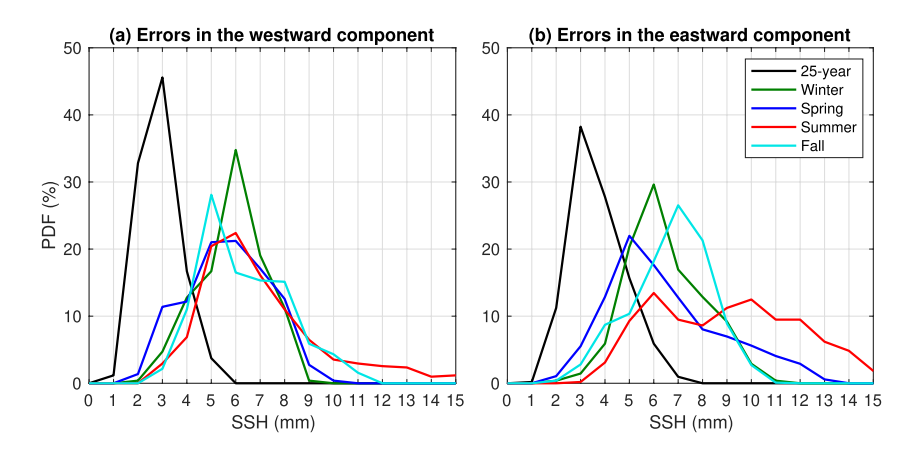


Figure A1. Model errors are indicated using background internal tide fields, which are constructed using the same satellite data and following the same mapping procedure, but with two background tidal periods ( $M_2 \pm 3$  min). The background fields are divided into westward (90–240°) and eastward (-80° to 60°) components. (f) Cross-beam model errors.



**Figure A2.** Histograms of the model errors estimated in Figure A1. (a) Westward component. (b) Eastward component. The errors in the 25-year-coherent model peak at 3 mm. The errors in the four seasonal fields peak around 6–8 mm.

ZHAO AND QIU 15 of 18

21699291, 2023, 3, Downloaded from https://agupubs

# **Data Availability Statement**

The satellite altimetry along-track data were downloaded from the Copernicus Marine Service (https://doi.org/10.48670/moi-00146). The satellite altimetry gridded data were also downloaded from the Copernicus Marine Service (https://doi.org/10.48670/moi-00148). The World Ocean Atlas 2013 is produced and made available by NOAA National Oceanographic Data Center (https://www.nodc.noaa.gov/OC5/woa13/). The seasonal internal tide models developed in this study are open to the oceanographic community (https://doi.org/10.6084/m9.figshare.19621311.v3).

#### Acknowledgments

This work was supported by the National Aeronautics and Space Administration (NASA) via projects NNX17AH57G and 80NSSC18K0771, and the National Science Foundation (NSF) via projects OCE1947592 and OCE2149028. The authors thank two anonymous reviewers for their constructive suggestions.

#### References

- Alford, M. H., Peacock, T., Mackinnon, J. A., Nash, J. D., Buijsman, M. C., Centurioni, L. R., et al. (2015). The formation and fate of internal waves in the South China Sea. *Nature*, 521(7550), 65–69. https://doi.org/10.1038/nature14399
- Bai, X., Liu, Z., Zheng, Q., Hu, J., Lamb, K. G., & Cai, S. (2019). Fission of shoaling internal waves on the northeastern shelf of the South China Sea. *Journal of Geophysical Research: Oceans*, 124(7), 4529–4545. https://doi.org/10.1029/2018JC014437
- Bij de Vaate, I., Vasulkar, A. N., Slobbe, D. C., & Verlaan, M. (2021). The influence of Arctic landfast ice on seasonal modulation of the M2 Tide. Journal of Geophysical Research: Oceans, 126(5), e2020JC016630. https://doi.org/10.1029/2020JC016630
- Buijsman, M. C., Arbic, B. K., Richman, J. G., Shriver, J. F., Wallcraft, A. J., & Zamudio, L. (2017). Semidiurnal internal tide incoherence in the equatorial Pacific. *Journal of Geophysical Research: Oceans*, 122(7), 5286–5305. https://doi.org/10.1002/2016JC012590
- Buijsman, M. C., Klymak, J. M., Legg, S., Alford, M. H., Farmer, D., MacKinnon, J. A., et al. (2014). Three-dimensional double-ridge internal tide resonance in Luzon Strait. *Journal of Physical Oceanography*, 44(3), 850–869. https://doi.org/10.1175/JPO-D-13-024.1
- Buijsman, M. C., McWilliams, J. C., & Jackson, C. R. (2010). East-west asymmetry in nonlinear internal waves from Luzon Strait. *Journal of Geophysical Research: Oceans*, 115(C10), C10057. https://doi.org/10.1029/2009JC006004
- Cao, A., Guo, Z., Lv, X., Song, J., & Zhang, J. (2017). Coherent and incoherent features, seasonal behaviors and spatial variations of internal tides
- in the northern South China Sea. *Journal of Marine Systems*, 172, 75–83. https://doi.org/10.1016/j.jmarsys.2017.03.005
  Cao, A., Guo, Z., Wang, S., Guo, X., & Song, J. (2022). Incoherence of the  $M_2$  and  $K_1$  internal tides radiated from the Luzon Strait under the
- influence of looping and leaping Kuroshio. *Progress in Oceanography*, 206, 102850. https://doi.org/10.1016/j.pocean.2022.102850 Chang, M.-H., Lien, R.-C., Lamb, K. G., & Diamessis, P. J. (2021). Long-term observations of shoaling internal solitary waves in the northern
- South China Sea. *Journal of Geophysical Research: Oceans*, 126(10), e2020JC017129. https://doi.org/10.1029/2020JC017129
  Chelton, D. B., de Szoeke, R. A., Schlax, M. G., El Naggar, K., & Siwertz, N. (1998). Geographical variability of the first baroclinic Rossby radius
- of deformation. Journal of Physical Oceanography, 28(3), 433–460. https://doi.org/10.1175/1520-0485(1998)028(0433:GVOTFB)2.0.CO;2 Chen, S., & Qiu, B. (2021). Sea surface height variability in the 30–120 km wavelength band from altimetry along-track observations. Journal of
- Geophysical Research: Oceans, 126(4), e2021JC017284. https://doi.org/10.1029/2021JC017284<br/>
  Colosi, J. A., & Munk, W. (2006). Tales of the venerable Honolulu tide gauge. Journal of Physical Oceanography, 36(6), 967–996. https://doi.org/10.1175/JPO2876.1
- Davis, K. A., Arthur, R. S., Reid, E. C., Rogers, J. S., Fringer, O. B., De Carlo, T. M., & Cohen, A. L. (2020). Fate of internal waves on a shallow shelf. *Journal of Geophysical Research: Oceans*, 125(5), e2019JC015377. https://doi.org/10.1029/2019JC015377
- DeCarlo, T. M., Karnauskas, K. B., Davis, K. A., & Wong, G. T. F. (2015). Climate modulates internal wave activity in the northern South China Sea. *Geophysical Research Letters*, 42(3), 831–838. https://doi.org/10.1002/2014GL062522
- Dunphy, M., & Lamb, K. G. (2014). Focusing and vertical mode scattering of the first mode internal tide by mesoscale eddy interaction. *Journal of Geophysical Research: Oceans*, 119(1), 523–536. https://doi.org/10.1002/2013JC009293
- Guo, Z., Cao, A., Lv, X., & Song, J. (2020). Impacts of stratification variation on the M<sub>2</sub> internal tide generation in Luzon Strait. *Atmosphere-Ocean*, 58(3), 206–218. https://doi.org/10.1080/07055900.2020.1767534
- Huang, X., Chen, Z., Zhao, W., Zhang, Z., Zhou, C., Yang, Q., & Tian, J. (2016). An extreme internal solitary wave event observed in the northern South China Sea. *Scientific Reports*, 6(1), 30041. https://doi.org/10.1038/srep30041
- Huang, X., Huang, S., Zhao, W., Zhang, Z., Zhou, C., & Tian, J. (2022). Temporal variability of internal solitary waves in the northern South China Sea revealed by long-term mooring observations. *Progress in Oceanography*, 201, 102716. https://doi.org/10.1016/j.pocean.2021.102716
- Huang, X., Wang, Z., Zhang, Z., Yang, Y., Zhou, C., Yang, Q., et al. (2018). Role of mesoscale eddies in modulating the semidiurnal internal tide: Observation results in the northern South China Sea. *Journal of Physical Oceanography*, 48(8), 1749–1770. https://doi.org/10.1175/
- Jan, S., Chern, C.-S., Wang, J., & Chiou, M.-D. (2012). Generation and propagation of baroclinic tides modified by the Kuroshio in the Luzon Strait. Journal of Geophysical Research: Oceans, 117(C2), C02019. https://doi.org/10.1029/2011JC007229
- Jan, S., Lien, R.-C., & Ting, C.-H. (2008). Numerical study of baroclinic tides in Luzon Strait. Journal of Oceanography, 64(5), 789–802. https://doi.org/10.1007/s10872-008-0066-5
- Kelly, S. M., & Nash, J. D. (2010). Internal-tide generation and destruction by shoaling internal tides. *Geophysical Research Letters*, 37(23), L23611. https://doi.org/10.1029/2010GL045598
- Kerry, C. G., Powell, B. S., & Carter, G. S. (2013). Effects of remote generation sites on model estimates of M<sub>2</sub> internal tides in the Philippine Sea. *Journal of Physical Oceanography*, 43(1), 187–204. https://doi.org/10.1175/JPO-D-12-081.1
- Kim, Y. Y., Qu, T., Jensen, T., Miyama, T., Mitsudera, H., Kang, H.-W., & Ishida, A. (2004). Seasonal and interannual variations of the North Equatorial Current bifurcation in a high-resolution OGCM. *Journal of Geophysical Research: Oceans*, 109(C3), C03040. https://doi.org/10.1029/2003JC002013
- Lamb, K. G., & Dunphy, M. (2018). Internal wave generation by tidal flow over a two-dimensional ridge: Energy flux asymmetries induced by a steady surface trapped current. *Journal of Fluid Mechanics*, 836, 192–221. https://doi.org/10.1017/jfm.2017.800
- Li, Q., & Farmer, D. M. (2011). The generation and evolution of nonlinear internal waves in the deep basin of the South China Sea. *Journal of Physical Oceanography*, 41(7), 1345–1363. https://doi.org/10.1175/2011JPO4587.1
- Lien, R.-C., Henyey, F., Ma, B., & Yand, Y. J. (2014). Large-amplitude internal solitary waves observed in the northern South China Sea: Properties and energetics. *Journal of Physical Oceanography*, 44(4), 1095–1115. https://doi.org/10.1175/JPO-D-13-088.1
- Liu, J., He, Y., Wang, D., Liu, T., & Cai, S. (2015). Observed enhanced internal tides in winter near the Luzon Strait. *Journal of Geophysical Research: Oceans*, 120(10), 6637–6652. https://doi.org/10.1002/2015JC011131

ZHAO AND QIU 16 of 18

- Locarnini, R. A., Mishonov, A. V., Antonov, J. I., Boyer, T. P., Garcia, H. E., Baranova, O. K., et al. (2013). World ocean atlas 2013 (Vol. 1). Temperature. NOAA Atlas NESDIS 73. Retrieved from http://data.nodc.noaa.gov/woa/WOA13/DOC/woa13 vol1.pdf
- Lyard, F. H., Allain, D. J., Cancet, M., Carrère, L., & Picot, N. (2021). FES2014 global ocean tide atlas: Design and performance. *Ocean Science*, 17(3), 615–649. https://doi.org/10.5194/os-17-615-2021
- Mercier, M. J., Gostiaux, L., Helfrich, K., Sommeria, J., Viboud, S., Didelle, H., et al. (2013). Large-scale, realistic laboratory modeling of M<sub>2</sub> internal tide generation at the Luzon Strait. Geophysical Research Letters, 40(21), 1–6. https://doi.org/10.1002/2013GL058064
- Müller, M., Cherniawsky, J. Y., Foreman, M. G. G., & von Storch, J.-S. (2012). Global M<sub>2</sub> internal tide and its seasonal variability from high resolution ocean circulation and tide modeling. Geophysical Research Letters, 39(19), L19607. https://doi.org/10.1029/2012GL053320
- Müller, M., Cherniawsky, J. Y., Foreman, M. G. G., & von Storch, J.-S. (2014). Seasonal variation of the M2 tide. *Ocean Dynamics*, 64(2), 159–177, https://doi.org/10.1007/s10236-013-0679-0
- Nan, F., Xue, H., & Yu, F. (2015). Kuroshio intrusion into the South China Sea: A review. Progress in Oceanography, 137, 314–333. https://doi.org/10.1016/j.pocean.2014.05.012
- Niwa, Y., & Hibiya, T. (2004). Three-dimensional numerical simulation of M<sub>2</sub> internal tides in the East China Sea. *Journal of Geophysical Research*, 109(C4), C04027. https://doi.org/10.1029/2003JC001923
- Park, J.-H., & Farmer, D. (2013). Effects of Kuroshio intrusions on nonlinear internal waves in the South China Sea during winter. *Journal of Geophysical Research*, 118(12), 7081–7094. https://doi.org/10.1002/2013JC008983
- Pickering, A., Alford, M., Nash, J., Rainville, L., Buijsman, M., Ko, D. S., & Lim, B. (2015). Structure and variability of internal tides in Luzon Strait. *Journal of Physical Oceanography*, 45(6), 1574–1594. https://doi.org/10.1175/JPO-D-14-0250.1
- Ponte, A. L., & Klein, P. (2015). Incoherent signature of internal tides on sea level in idealized numerical simulations. Geophysical Research Letters, 42(5), 1520–1526. https://doi.org/10.1002/2014GL062583
- Pujol, M.-I., Faugère, Y., Taburet, G., Dupuy, S., Pelloquin, C., Ablain, M., & Picot, N. (2016). DUACS DT2014: The new multi-mission altim-
- eter data set reprocessed over 20 years. Ocean Science, 12(5), 1067–1090. https://doi.org/10.5194/os-12-1067-2016
  Qiu, B., & Lukas, R. (1996). Seasonal and interannual variability of the North Equatorial Current, the Mindanao Current, and the Kuroshio along
- the Pacific western boundary. *Journal of Geophysical Research: Oceans*, 101(C5), 12315–12330. https://doi.org/10.1029/95JC03204
  Ray, R. D. (2022). Technical note: On seasonal variability of the M<sub>2</sub> tide. *Ocean Science*, 18(4), 1073–1079. https://doi.org/10.5194/
- os-18-1073-2022
  Ray, R. D., & Byrne, D. A. (2010). Bottom pressure tides along a line in the southeast Atlantic Ocean and comparisons with satellite altimetry.
- Ray, R. D., & Byrne, D. A. (2010). Bottom pressure tides along a line in the southeast Atlantic Ocean and comparisons with satellite altimetry *Ocean Dynamics*, 60(5), 1167–1176. https://doi.org/10.1007/s10236-010-0316-0
- Ray, R. D., & Mitchum, G. T. (1996). Surface manifestation of internal tides generated near Hawaii. *Geophysical Research Letters*, 23(16), 2101–2104. https://doi.org/10.1029/96GL02050
- Ray, R. D., & Mitchum, G. T. (1997). Surface manifestation of internal tides in the deep ocean: Observations from altimetry and island gauges. Progress in Oceanography, 40(1), 135–162. https://doi.org/10.1016/S0079-6611(97)00025-6
- Ray, R. D., & Susanto, R. D. (2016). Tidal mixing signatures in the Indonesian Seas from high-resolution sea surface temperature data. Geophysical Research Letters, 43(15), 8115–8123. https://doi.org/10.1002/2016GL069485
- Ray, R. D., & Zaron, E. D. (2011). Non-stationary internal tides observed with satellite altimetry. Geophysical Research Letters, 38(17), L17609. https://doi.org/10.1029/2011GL048617
- Ray, R. D., & Zaron, E. (2016). M<sub>2</sub> internal tides and their observed wavenumber spectra from satellite altimetry. *Journal of Physical Oceanog-raphy*, 46(1), 3–22. https://doi.org/10.1175/JPO-D-15-0065.1
- Savage, A. C., Waterhouse, A. F., & Kelly, S. M. (2020). Internal tide nonstationarity and wave-mesoscale interactions in the Tasman Sea. *Journal of Physical Oceanography*, 50(10), 2931–2951. https://doi.org/10.1175/JPO-D-19-0283.1
- Shakespeare, C. J., & Hogg, A. M. (2019). On the momentum flux of internal tides. *Journal of Physical Oceanography*, 49(4), 993–1013. https://doi.org/10.1175/JPO-D-18-0165.1
- Smith, W. H. F., & Sandwell, D. T. (1997). Global sea floor topography from satellite altimetry and ship depth soundings. Science, 277(5334), 1956–1962. https://doi.org/10.1126/science.277.5334.1956
- Taburet, G., Sanchez-Roman, A., Ballarotta, M., Pujol, M.-I., Legeais, J.-F., Fournier, F., et al. (2019). DUACS DT2018: 25 years of reprocessed sea level altimetry products. *Ocean Science*, 15(5), 1207–1224. https://doi.org/10.5194/os-15-1207-2019
- Ubelmann, C., Carrere, L., Durand, C., Dibarboure, G., Faugère, Y., Ballarotta, M., et al. (2022). Simultaneous estimation of ocean mesoscale and coherent internal tide sea surface height signatures from the global altimetry record. *Ocean Science*, 18(2), 469–481. https://doi.org/10.5194/os-18-469-2022
- Wang, X., Peng, S., Liu, Z., Huang, R. X., Qian, Y.-K., & Li, Y. (2016). Tidal mixing in the South China Sea: An estimate based on the internal tide energetics. *Journal of Physical Oceanography*, 46(1), 107–124. https://doi.org/10.1175/JPO-D-15-0082.1
- Wu, C.-R., Wang, Y.-L., Lin, Y.-F., & Chao, S.-Y. (2017). Intrusion of the Kuroshio into the South and East China Seas. Scientific Reports, 7(1), 7895. https://doi.org/10.1038/s41598-017-08206-4
- Xie, J., Fang, W., He, Y., Chen, Z., Liu, G., Gong, Y., & Cai, S. (2021). Variation of internal solitary wave propagation induced by the typical oceanic circulation patterns in the northern South China Sea deep basin. *Geophysical Research Letters*, 48(15), e2021GL093969. https://doi.org/10.1029/2021GL093969
- Xu, Z., Wang, Y., Liu, Z., McWilliams, J. C., & Gan, J. (2021). Insight into the dynamics of the radiating internal tide associated with the Kuroshio Current. *Journal of Geophysical Research: Oceans*, 126(6), e2020JC017018. https://doi.org/10.1029/2020JC017018
- Xu, Z., Yin, B., Hou, Y., & Liu, A. K. (2014). Seasonal variability and north–south asymmetry of internal tides in the deep basin west of the Luzon Strait. Journal of Marine Systems, 134, 101–112. https://doi.org/10.1016/j.jmarsys.2014.03.002
- Yuan, D., Han, W., & Hu, D. (2006). Surface Kuroshio path in the Luzon Strait area derived from satellite remote sensing data. *Journal of Geophysical Research*, 111(C11), C11007. https://doi.org/10.1029/2005JC003412
- Zaron, E. D. (2017). Mapping the nonstationary internal tide with satellite altimetry. *Journal of Geophysical Research: Oceans*, 122(1), 539–554. https://doi.org/10.1002/2016JC012487
- Zaron, E. D. (2019). Baroclinic tidal sea level from exact-repeating mission altimetry. *Journal of Physical Oceanography*, 49(1), 193–210. https://doi.org/10.1175/JPO-D-18-0127.1
- Zaron, E. D., Capuano, T. A., & Koch-Larrouy, A. (2023). Fortnightly variability of chl a in the Indonesian Seas. Ocean Science, 19(1), 43–55. https://doi.org/10.5194/os-19-43-2023
- Zaron, E. D., & Egbert, G. D. (2014). Time-variable refraction of the internal tide at the Hawaiian Ridge. *Journal of Physical Oceanography*, 44(2), 538–557. https://doi.org/10.1175/JPO-D-12-0238.1
- Zaron, E. D., Musgrave, R. C., & Egbert, G. D. (2022). Baroclinic tidal energetics inferred from satellite altimetry. *Journal of Physical Oceanog-raphy*, 52(5), 1015–1032. https://doi.org/10.1175/JPO-D-21-0096.1

ZHAO AND QIU 17 of 18



# Journal of Geophysical Research: Oceans

- 10.1029/2022JC019281
- Zaron, E. D., & Ray, R. D. (2018). Aliased tidal variability in mesoscale sea level anomaly maps. *Journal of Atmospheric and Oceanic Technology*, 35(12), 2421–2435. https://doi.org/10.1175/JTECH-D-18-0089.1
- Zhai, R.-W., Chen, G.-Y., Liang, C.-R., Shang, X.-D., & Xie, J.-S. (2020). The influence of ENSO on the structure of internal tides in the Xisha area. *Journal of Geophysical Research: Oceans*, 125(3), e2019JC015405. https://doi.org/10.1029/2019JC015405
- Zhao, Z. (2014). Internal tide radiation from the Luzon Strait. Journal of Geophysical Research: Oceans, 119(8), 5434–5448. https://doi.org/10.1024/2014JC010014
- Zhao, Z. (2016). Internal tide oceanic tomography. Geophysical Research Letters, 43(17), 9157–9164. https://doi.org/10.1002/2016GL070567
- Zhao, Z. (2020). Southward internal tides in the northeastern South China Sea. Journal of Geophysical Research: Oceans, 125(11), e2020JC01654. https://doi.org/10.1029/2020JC016554
- Zhao, Z. (2021). Seasonal mode-1 M<sub>2</sub> internal tides from satellite altimetry. *Journal of Physical Oceanography*, 51, 3015–3035. https://doi.org/10.1175/JPO-D-21-0001.1
- Zhao, Z. (2022). Development of the yearly mode-1 M<sub>2</sub> internal tide model in 2019. Journal of Atmospheric and Oceanic Technology, 39(4), 463–478. https://doi.org/10.1175/JTECH-D-21-0116.1
- Zhao, Z., & Alford, M. H. (2009). New altimetric estimates of mode-1 M<sub>2</sub> internal tides in the central North Pacific Ocean. *Journal of Physical Oceanography*, 39(7), 1669–1684. https://doi.org/10.1175/2009JPO3922.1
- Zhao, Z., Alford, M. H., Girton, J. B., Rainville, L., & Simmons, H. L. (2016). Global observations of open-ocean mode-1 M<sub>2</sub> internal tides. Journal of Physical Oceanography, 46(6), 1657–1684. https://doi.org/10.1175/JPO-D-15-0105.1
- Zhao, Z., Klemas, V., Zheng, Q., & Yan, X.-H. (2004). Remote sensing evidence for baroclinic tide origin of internal solitary waves in the north-eastern South China Sea. *Geophysical Research Letters*, 31(6), L06302. https://doi.org/10.1029/2003GL019077
- Zheng, Q., Susanto, R. D., Ho, C.-R., Song, Y. T., & Xu, Q. (2007). Statistical and dynamical analyses of generation mechanism of solitary internal waves in the northern South China Sea. *Journal of Geophysical Research*, 112(C3), C03021. https://doi.org/10.1029/2006JC003551
- Zweng, M., Reagan, J., Antonov, J., Locarnini, R., Mishonov, A., Boyer, T., et al. (2013). World ocean atlas 2013 (Vol. 2). Salinity. NOAA Atlas NESDIS 74. Retrieved from http://data.nodc.noaa.gov/woa/WOA13/DOC/woa13\_vol2.pdf

ZHAO AND QIU 18 of 18